**Rare Metal Materials and Engineering**
Volume 52, Issue 5, May 2023
Available online at www.rmme.ac.cn

Science Press

**Cite this article as**: Cui Xiaoming, Liang Shaobo, Zhao Xueping, et al. Microstructure Evolution of Al-Mn-Mg-Sc-Zr Alloy Prepared by Selective Laser Melting Before and After Heat Treatment[J]. Rare Metal Materials and Engineering, 2023, 52(05): 1603-1609.

ARTICLE

# Microstructure Evolution of Al-Mn-Mg-Sc-Zr Alloy Prepared by Selective Laser Melting Before and After Heat Treatment

**Cui Xiaoming, Liang Shaobo, Zhao Xueping, Cui Hao, Liu Fei, Du Zhaoxin, Bai Pucun**

*School of Materials Science and Engineering, Inner Mongolia University of Technology, Hohhot 010051, China*

**Abstract:** Al-Mn-Mg-Sc-Zr alloy was prepared by selective laser melting (SLM) technique. The microstructure of Al-Mn-Mg-Sc-Zr alloy before and after heat treatment was characterized by X-ray diffractometer, scanning electron microscope, energy dispersive spectrometer, and transmission electron microscope, and the hardness of the alloy was tested. Results show that the microstructure of as-deposited alloy is mainly composed of $\alpha$-Al, $Al_6Mn$, and primary $Al_3Sc$ phases. The SLMed molten pool presents the fish-scale shape, and a large number of fine equiaxed crystals are formed near the fusion line of molten pool with average grain size of about 0.57 μm. The center of the molten pool is composed of columnar crystals with average width of about 0.48 μm. The rodlike $Al_6Mn$ phase is mainly distributed along the grain boundary, and a small amount of granular primary $Al_3Sc$ phase exists inside the grain, which indicates that the primary $Al_3Sc$ can be used as heterogeneous nuclear particle to refine the $\alpha$-Al matrix. After heat treatment, the size of equiaxed crystals and the width of columnar crystals in the molten pool are increased, and a large number of fine and dispersed secondary $Al_3Sc$ particles are precipitated in the structure. The hardness test results show that the hardness of the alloy is increased firstly and then decreased with prolong the aging durations at different temperatures. Compared with that of the as-deposited alloy, the hardness of the alloy after peak aging (325 °C/180 min) heat treatment increases by about 30%, reaching 1813.0 MPa.

**Key words:** Al-Mn-Mg-Sc-Zr alloy; selective laser melting technique; rare earth Sc; heat treatment; microstructure

As an industrial-scale structural engineering material, aluminum alloys have been widely used in aerospace and automobile manufacturing due to their advantages of high specific strength, high specific stiffness, excellent casting performance, and fine recyclability[1–3]. Due to the slow cooling rate of the metal during the forming process, aluminum alloys formed by the traditional casting process usually have coarse grains, defects, and element segregation[4], which restricts the application range of the aluminum alloy. With the development of industrial modernization, various new requirements for the properties of aluminum alloys have been proposed. For the complex and precise structural parts of aluminum alloys, the traditional casting method can no longer meet the actual requirements in the manufacture of aerospace equipment[5]. Selective laser melting (SLM) technique has the characteristics of rapid cooling, which can realize the direct forming of complex structural parts of aluminum alloys with high performance and high precision, thus expanding the application filed of aluminum alloys[6–7]. Currently, the aluminum alloys used in SLM technique are mainly Al-Si, Al-Mg, Al-Cu, and aluminum-based composites[8]. Zhao et al[9] prepared the AlSi10Mg alloy by SLM technique and studied the effects of stress release annealing and friction stir on the microstructure and properties of the alloy. Results show that after stress release annealing and friction stir treatments, the Si phase of AlSi10Mg alloy is spheroidized, the ductility is increased by four times, but the strength is reduced by 30%. Geng et al[10] prepared the Al-14.4Mg-0.33Sc-0.19Zr alloy by SLM technique and studied the effects of different process parameters and aging treatments on the formability, microstructure, and mechanical properties of the alloy. Results show that the relative density of the formed specimen is 98.6% under the high laser power. The microstructure of the prepared alloy is composed of equiaxed grains near the fusion line and coarse grains in the center of the molten pool. The hardness and yield strength reaches the maximum under the

Received date: September 01, 2022
Foundation item: Science and Technology Plan Project of Inner Mongolia (201802029); Major Science and Technology Projects of Inner Mongolia Autonomous Region (zdzx2018031); Graduate Research Innovation Project of Inner Mongolia Autonomous Region (S20210180Z)
Corresponding author: Bai Pucun, Ph. D., Professor, School of Materials Science and Engineering, Inner Mongolia University of Technology, Hohhot 010051, Tel: 0086-471-6576221, E-mail: pcbai@ imut.edu.cn

condition of 350 °C/1 h. Compared with Al-Si and Al-Mg alloys, the Al-Cu alloys are prone to hot cracks and burning loss, which affect the quality of the prepared specimens. Xu et al[11] prepared the Al-Cu-Mg alloys modified by Li and Zr elements (Al-4Cu-1Li-0.4Mg-0.5Zr) by SLM technique, and the microstructure, forming defects, and microhardness of the alloy were studied. Results show that the microstructure of the prepared alloy is composed of equiaxed and columnar crystals, and obvious cracks and pores exist in the alloy. The microhardness is increased with increasing the laser energy density. However, the Al-Mn alloys prepared by SLM technique are rarely reported. Al-Mn alloys have high plasticity and good welding performance, which is suitable for SLM treatment. The strength of aluminum alloy can be improved by adding manganese. The additive manganese may dissolve in the matrix or participate in the formation of fine precipitates, thereby providing solid solution strengthening and precipitation strengthening effects[12]. It is reported that the addition of rare earth (RE) elements can inhibit the recrystallization of Al-Mn alloys and improve the mechanical properties of Al-Mn alloys. In addition, the $L1_2$-type $Al_3RE$ particles are formed in the aluminum alloy after RE addition. During the heat treatment of aluminum alloy, $Al_3RE$ particles can effectively pin the dislocations and subgrain boundaries, thus inhibiting the recrystallization and grain growth[13].

In this research, the Al-Mn-Mg-Sc-Zr alloys were prepared by SLM technique. The microstructures of the alloys before and after heat treatment were studied. The existence form and mechanism of Sc element were discussed. The effect of heat treatment on the stability of precipitated particles was analyzed, which provides guidance for the development of aluminum alloys for 3D printing or heat treatment.

## 1 Experiment

The raw material was Al-Mn-Mg-Sc-Zr alloy powder with sphericity of 0.85. The minimum, maximum, and average diameters of powder were about 18.0, 60.4, and 32.0 μm, respectively. The chemical composition of the powder is shown in Table 1. The SLM treatment was conducted by Renishaw RenAM 500 E equipment (Renishaw Company, UK). Argon was introduced as the protective gas during the working process. The schematic diagram and appearance of as-deposited specimens are shown in Fig. 1 (BD indicates the deposition direction). The specimen microstructures were characterized by Axio Imager A1 m Zeiss optical microscope (OM), FEI Quanta 650 scanning electron microscope (SEM), X-ray diffractometer (XRD), and Talos F200 X transmission electron microscope (TEM). The OTF-1200X tube furnace was used for aging treatment. The aging temperature was 325, 375, 425, and 475 °C, and the aging time was 24 h. The hardness of the specimens was tested by HVS-30Z/LCD Vickers hardness tester.

**Table 1 Chemical composition of Al-Mn-Mg-Sc-Zr alloy powder (wt%)**

| Mn | Mg | Sc | Zr | Fe | Si | Al |
|---|---|---|---|---|---|---|
| 4.55 | 1.19 | 0.94 | 0.43 | 0.07 | 0.04 | Bal. |

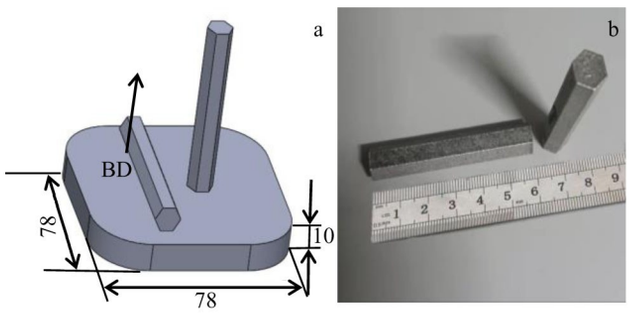


Fig.1 Schematic diagram (a) and appearance (b) of as-deposited specimens by SLM technique

## 2 Results and Discussion

### 2.1 Microstructure analysis of as-deposited alloy

Fig. 2a shows the overall OM microstructures of as-deposited alloy specimen. BD of the alloy specimen is parallel to the *Z* axis. In order to investigate the microstructure and formability of the as-deposited alloy specimen, the typical surfaces of *XY* and *YZ* planes were observed for analysis. Fig. 2b shows OM microstructure of the alloy specimen along *XY* plane. It can be seen that the width of the molten pool formed by SLM technique is about 150 μm. The projection angle of the molten pool of the two adjacent sedimentary layers in the alloy specimen along *XY* plane is 67°, i.e., the angle between the *N* layer and the *N*+1 layer is 67°. This is due to the deflection (67°) of the laser scanning path direction of the two adjacent cladding layers during the forming process. Meanwhile, it can be seen that under the scanning path deflection of 67°, the obtained specimen has a dense structure, no obvious holes or defects can be observed, and the specimen forming quality is good. Fig. 2c shows OM microstructure of the alloy specimen along *YZ* plane. The microstructure of the formed part is similar to the fish-scale shape, and each individual fish-scale indicates a molten pool. The projection morphologies of the molten pool along the width direction on the *YZ* surface are different, which is due to the deflection of 67° between the laser beam path of adjacent cladding layers, and the angle between the laser scanning path of cladding layer and *YZ* surface is also different for different cladding layers. Three molten pools with different angles between the molten pool and *YZ* plane were established, as shown in Fig.2d–2f.

### 2.2 Phase analysis of as-deposited alloy

XRD analysis results of the as-deposited alloy specimen are shown in Fig. 3. The alloy specimen is mainly composed of $\alpha$-Al and $Al_6Mn$ phases. $Al_3Sc$ phase may also exist in the alloy. Because $Al_3Sc$ and $\alpha$-Al phases both have the face-centered cubic structure and their crystal plane spacing is very close, the diffraction peaks of $Al_3Sc$ phase may overlap with those of the $\alpha$-Al phase. Because the $Al_3Sc$ phase is far less than $\alpha$-Al phase, the existence of $Al_3Sc$ phase can hardly be

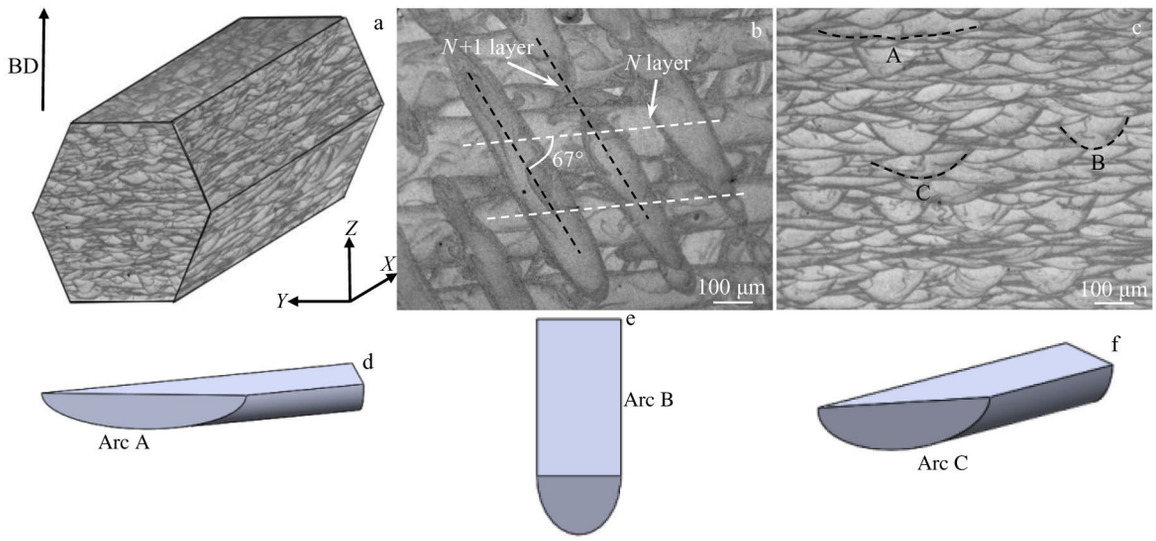


Fig.2 OM microstructures of as-deposited alloy specimen of overall view (a), along *XY* plane (b), and along *YZ* plane (c); schematic diagrams of arc A (d), arc B (e), and arc C (f) of single-pass molten pool in Fig.2c

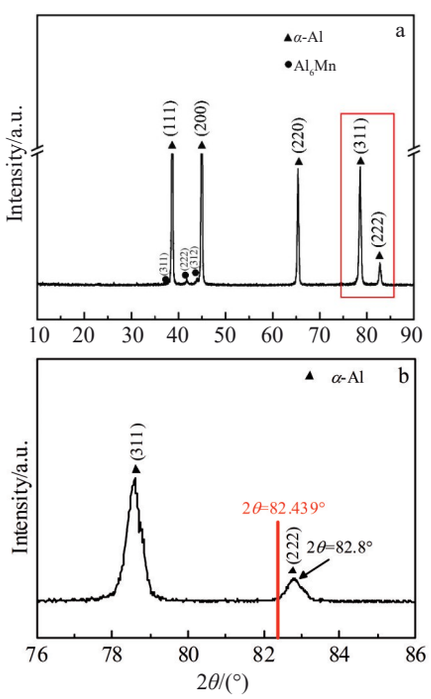


Fig.3 XRD patterns of as-deposited alloy specimen: (a) $2\theta$=10°–90°; (b) $2\theta$=76°–86°

determined by XRD. According to Fig.3b, the diffraction peak of the $\alpha$-Al phase in the as-deposited alloy specimen shifts, which indicates that some alloying elements dissolve in the aluminum matrix, thus forming the $\alpha$-Al solid solution and resulting in the distortion of $\alpha$-Al lattice.

### 2.3 SEM analysis of as-deposited specimens before and after heat treatment

The as-deposited alloy specimens before and after heat treatment (aging treatment at 375 ° C for 40 min) were observed by scanning transmission electron microscope (STEM), as shown in Fig. 4. Fig. 4a and Fig. 4b show STEM morphologies of as-deposited alloy specimen near the fusion line on *YZ* surface before and after heat treatment, respectively. The microstructure near the fusion line of the as-deposited alloy specimen is mainly composed of fine and uniform equiaxed crystals. The gray-white $Al_6Mn$ secondary phase is mainly distributed along the grain boundary. Fine $Al_3Sc$ particles can be observed inside the grains, as shown in Fig. 4a, which indicates that the preferentially precipitated $Al_3Sc$ compound of high melting point can act as the heterogeneous nucleation core to refine the $\alpha$-Al microstructure. After aging treatment (Fig. 4b), the microstructure near the fusion line in the molten pool is still composed of fine equiaxed crystals, which are mainly distributed along the grain boundary of $Al_6Mn$ phase. The size and shape change slightly. It is worth noting that a large number of fine dispersed precipitates are produced in the $\alpha$-Al grains after aging treatment. The grain size near the fusion line of molten pool along *YZ* plane of the as-deposited and as-aged alloy specimens was measured. It can be seen that the equiaxed grain size of the as-deposited alloy specimen is 0.3–1.1 μm, and the average grain size is about 0.57 μm. After aging treatment, the equiaxed grain size increases slightly as 0.4–1.4 μm, and the average grain size is about 0.81 μm.

Fig. 4d and 4e show STEM microstructures inside the molten pool along *YZ* plane of the as-deposited and aged alloy specimens, respectively. It can be seen that the molten pool microstructure of the as-deposited alloy specimen is mainly composed of columnar crystals, and the $Al_6Mn$ phase distributed along the grain boundary is rod-shaped or granular. After aging treatment (Fig. 4e), a large number of fine dispersed precipitated particles appear inside the grains.

Similarly, the size and width of columnar crystals in the center of the molten pool of the as-deposited and as-aged alloy specimens along *YZ* plane were measured, and the

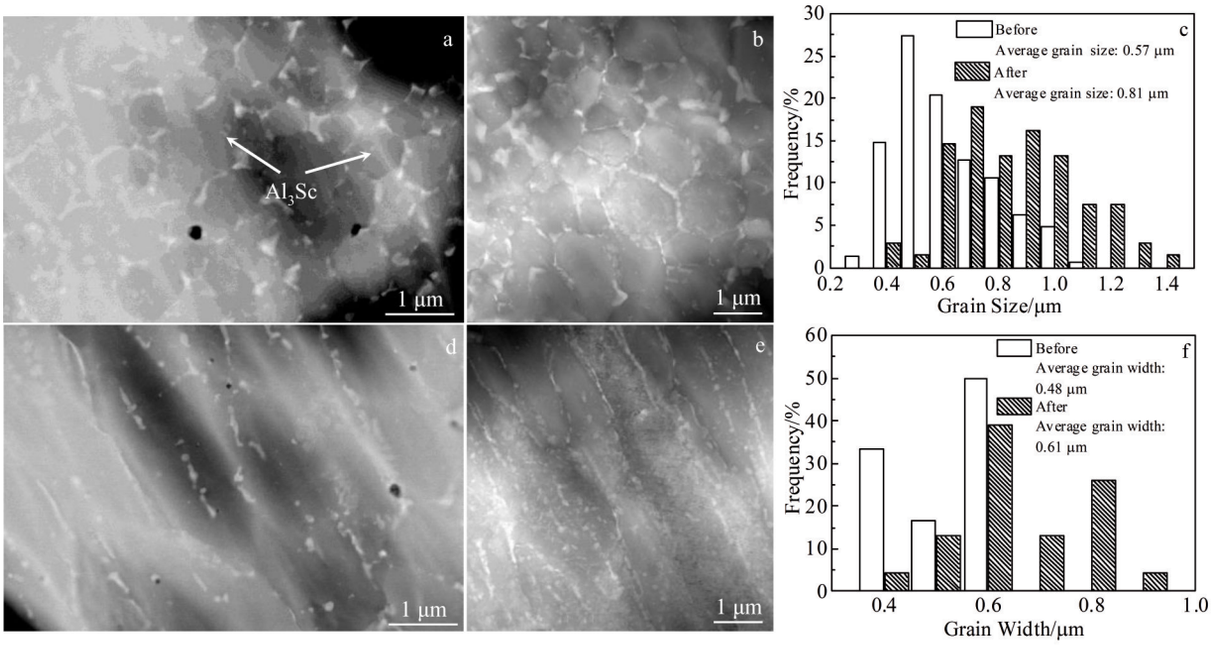


Fig.4 STEM microstructures near the fusion line (a, d) and inside the molten pool (b, e) before (a–b) and after (d–e) heat treatment at 375 °C for 40 min; distributions of grain size (c) and grain width (f) of alloy specimens before and after heat treatment

results are shown in Fig.4c and 4f. The width of as-deposited columnar crystals is 0.4 – 0.6 μm with the average width of about 0.48 μm. After aging treatment, the width of columnar crystals is from 0.4 μm to 0.9 μm, and the average width is about 0.61 μm.

### 2.4 TEM analysis of $Al_6Mn$ phase

Fig. 5a shows TEM image of $Al_6Mn$ phase in the as-deposited alloy specimen. As shown in Fig.5a, the dark gray rod-like and granular secondary phases are mainly distributed along the grain boundary. Fig. 5b shows the secondary phase observed by high-resolution TEM (HRTEM). The white rectangular area in Fig. 5b was treated by fast Fourier transform (FFT), and the corresponding selected area diffraction pattern (SAED) is shown in Fig.5c. It can be seen that the phase is $Al_6Mn$ and the crystal band axis is $[0\bar{1}2]$. A large number of dislocations exist in the as-deposited alloy specimen, and the dislocation pile-up is generated around the $Al_6Mn$ phase, which indicates that the $Al_6Mn$ can hinder the

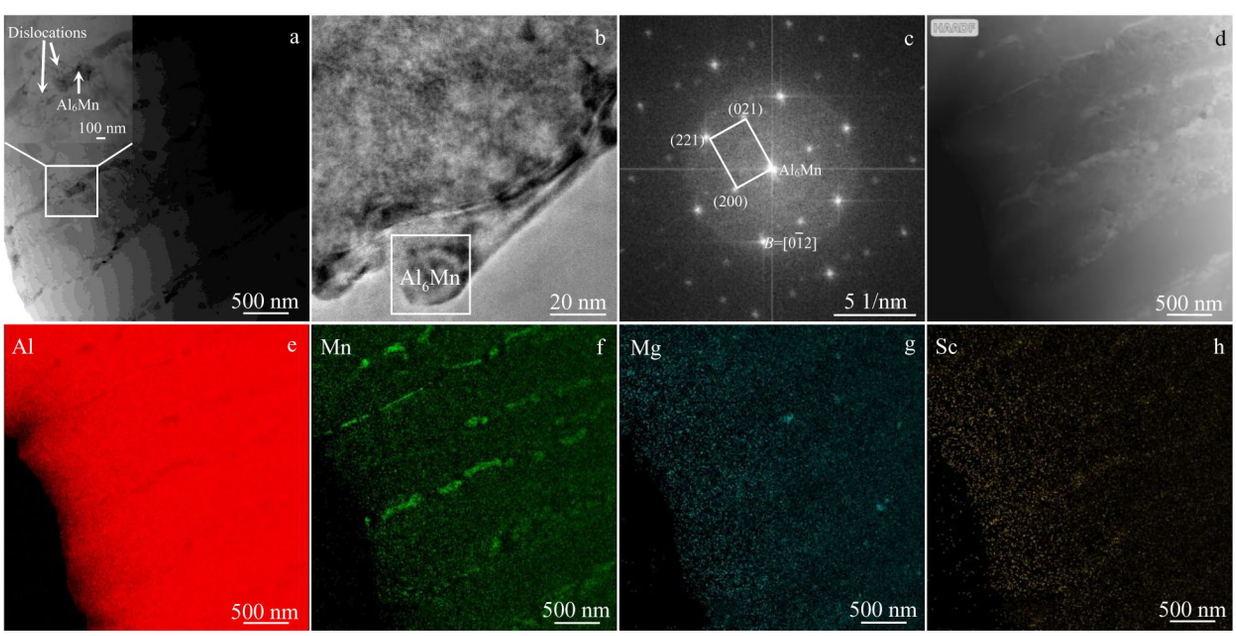


Fig.5 TEM image (a), HRTEM image (b), and corresponding SAED pattern (c) of $Al_6Mn$ phases in as-deposited alloy specimen; HAADF image (d) and corresponding EDS element distributions of Al (e), Mn (f), Mg (g), and Sc (h) of as-deposited alloy specimen

dislocation movement and cause stress concentration. In addition, the defects, such as high-density dislocations, in SLMed aluminum alloys can be used as channels for atomic diffusion to promote the nucleation and growth of precipitated phases during heat treatment of aluminum alloys[14]. Fig.5d shows the corresponding high-angle annular dark field (HAADF) image of the alloy specimen, and the corresponding EDS element distributions are shown in Fig.5e–5h. It can be seen that the rod-like and granular secondary phases in the alloy specimen are mainly enriched by Al and Mn elements. Thus, the phase is determined as $Al_6Mn$ phase. Mg and Sc elements exist in the $\alpha$-Al matrix with uniform distribution, indicating that some Mg and Sc elements dissolve in the $\alpha$-Al matrix.

Fig. 6a shows TEM image of $Al_6Mn$ phase in the alloy specimen after aging treatment at 375 °C for 40 min. The dark gray rod-like and granular secondary phases exist in the alloy specimen. After aging treatment, the dislocation density in the alloy specimen decreases, indicating that some stress is released. In addition, the edges of the rod-like and granular $Al_6Mn$ phases are blunt, and their contours become more rounded, which can alleviate the stress concentration around $Al_6Mn$ phase. Fig. 6b shows HRTEM image of white rectangular area in Fig. 6a. Based on the high-resolution contrast between the secondary phase and the matrix, no coherent relationship exists between them. SAED pattern corresponding to Fig.6b is shown in Fig.6c. It can be seen that the spots in Fig. 6c are clear and sharp, and the secondary phase can be determined as $Al_6Mn$ phase with crystal band axis of $[1\bar{3}0]$. Fig.6d shows the HAADF image corresponding to the alloy microstructure in Fig. 6a, and EDS element distribution results are shown in Fig.6e–6h. The bright white fine particle phase (yellow circles in Fig. 6d) are mainly enriched by Al and Sc elements, indicating the $Al_3Sc$ primary phase. The rod-like and granular secondary phases are mainly enriched by Al and Mn elements, suggesting the $Al_6Mn$ phase. The Mg element is uniformly distributed in the $\alpha$-Al matrix, indicating that some Mg dissolves in the matrix after aging treatment.

### 2.5 TEM analysis of $Al_3Sc$ phase

Fig.7a shows HRTEM image of $Al_3Sc$ primary phase in the equiaxed crystal near the fusion line of the as-deposited alloy specimen. Fig. 7b shows the magnified image of rectangular area in Fig.7a. According to Fig.7b, the secondary phase with diameter of about 15 nm can be clearly observed, and it can be determined as $Al_3Sc$ phase with band axis of [001], as shown in Fig.7c. The relationship between $Al_3Sc$ and $\alpha$-Al phases is $[001]_{Al_3Sc}//[001]_{\alpha\text{-Al}}$. The crystal structure of $Al_3Sc$ and $\alpha$-Al phases is face-centered cubic structure, and their lattice constants are $a=b=c=0.408\ 94$ nm and $a=b=c=0.404\ 94$ nm, respectively. The mismatch between $Al_3Sc$ and $\alpha$-Al phases is 0.99%, which is closely related to the heterogeneous nucleation. When the mismatch is less than 10%, the secondary phase may become the core of the heterogeneous nucleation. When the mismatch is less than 5%, the heterogeneous nucleation is in the dominate position[15]. Therefore, the $Al_3Sc$ primary phase produced in this research can be used as the heterogeneous nucleation particle of $\alpha$-Al matrix. During the forming process, the $Al_3Sc$ primary phase can enhance the nucleation of $\alpha$-Al phase, thus promoting the grain refinement.

Fig.8a shows HRTEM image of the secondary precipitation particles in the alloy specimen after aging treatment at 375 °C for 40 min. Many circular nanoparticle phases are uniformly

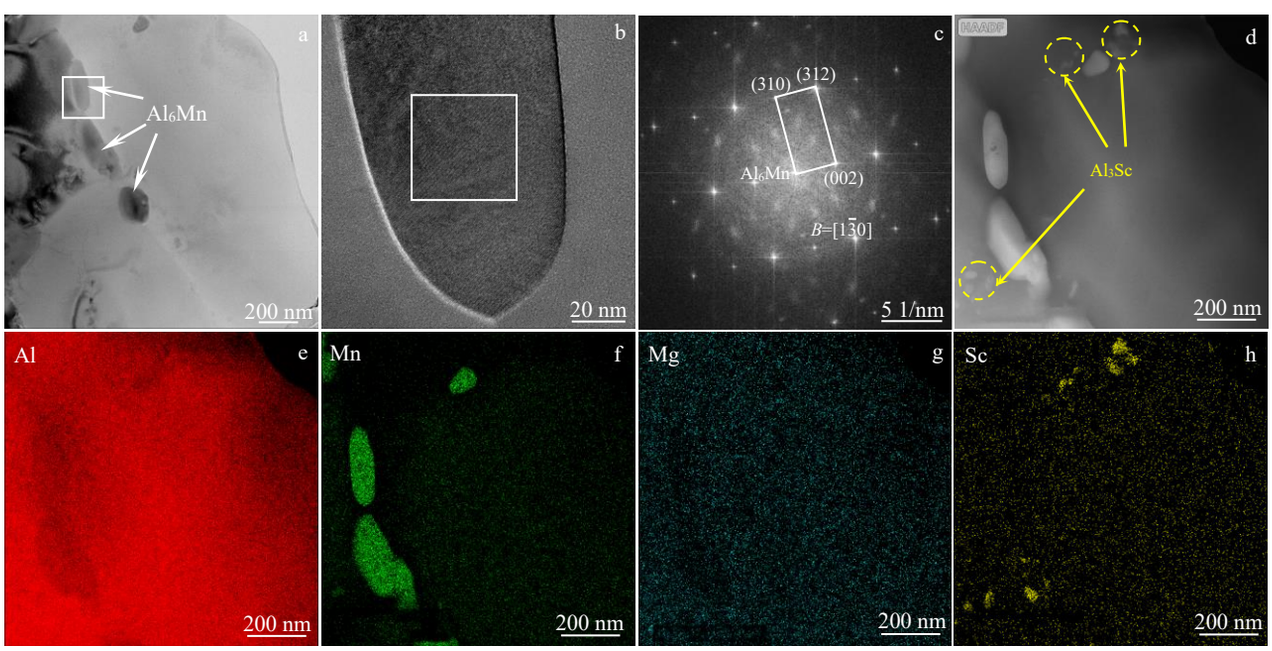


Fig.6 TEM image (a), HRTEM image (b), and corresponding SAED pattern (c) of $Al_6Mn$ phase in as-aged alloy specimen at 375 °C for 40 min; HAADF image (d) and corresponding EDS element distributions of Al (e), Mn (f), Mg (g), and Sc (h) of as-aged alloy specimen at 375 °C for 40 min

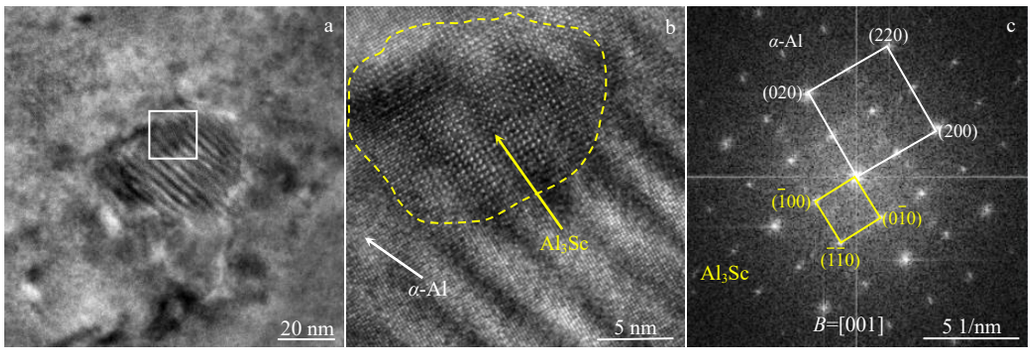


Fig.7 HRTEM image of $Al_3Sc$ primary phase in as-deposited alloy specimen (a); magnified HRTEM image (b) and corresponding SAED pattern (c) of rectangular area in Fig.7a

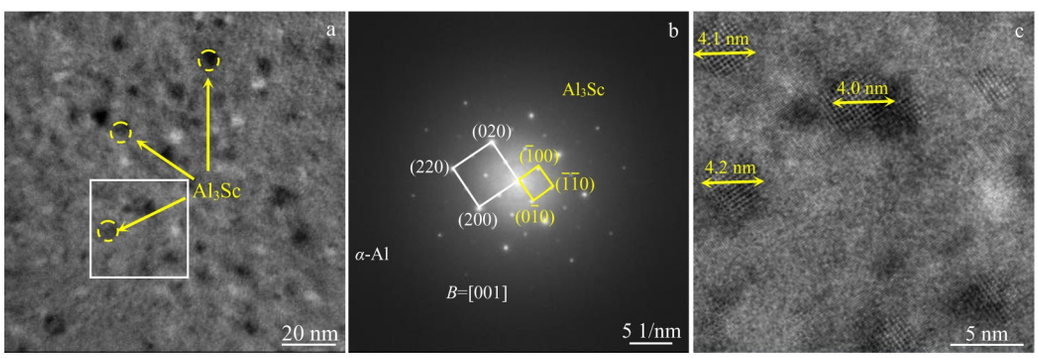


Fig.8 HRTEM image (a) and corresponding SAED pattern (b) of $Al_3Sc$ primary phase in as-aged alloy specimen at 375 °C for 40 min; magnified HRTEM image of rectangular area in Fig.8a (c)

distributed, as indicated by the yellow arrows in Fig. 8a. A large number of dispersed $Al_3Sc$ secondary nanoparticles are precipitated in the $\alpha$-Al matrix after aging treatment. Fig. 8b shows SAED pattern corresponding to Fig. 8a. It can be seen that the circular particle phase in Fig. 8a is $Al_3Sc$ and the crystal band axis is [001]. The microstructure around the $Al_3Sc$ particles is $\alpha$-Al phase. The $Al_3Sc$ secondary precipitation particles and $\alpha$-Al phase still have the relationship of $[001]_{Al_3Sc}//[001]_{\alpha\text{-Al}}$. According to Fig. 8c, the average size of $Al_3Sc$ precipitate is about 4 nm, which indicates that the $Al_3Sc$ precipitate particles have good thermal stability. Compared with those in the as-deposited alloy specimen, the $Al_3Sc$ precipitated particles in the $\alpha$-Al matrix of the as-aged alloy specimen present the characteristics of large quantity, small size, and dispersed distribution, which may be due to the high-density dislocations generated by the as-deposited alloy. The diffusion of Al and Sc atoms provides kinetic conditions to promote the precipitation of $Al_3Sc$ particles. The precipitated nano-sized $Al_3Sc$ particles can effectively pin the dislocation and hinder the further movement of dislocations, thereby improving the mechanical properties of the alloy specimen.

### 2.6 Hardness

Fig. 9 shows the hardness curves of the alloy specimens under different aging processes. The hardness is increased firstly and then decreased with the aging treatment proceeding. Besides, the higher the aging temperature, the shorter the duration for the alloy specimen to reach the peak hardness. After aging at 325 °C for 180 min (peak aging), the hardness of the alloy specimen is the highest of 1813.0 MPa, which is 30% higher than that of as-deposited alloy specimen. It is worth noting that when the aging temperature is lower than 375 ° C, the hardness loss of the over-aging alloy specimen is small. However, when the aging temperature is higher than 375 °C, the hardness of alloy specimen after over-aging treatment decreases rapidly and significantly, which is even far lower than that of the as-deposited alloy specimen. This may be due to the fact that with increasing the aging temperature, the residual stress in the alloy is gradually

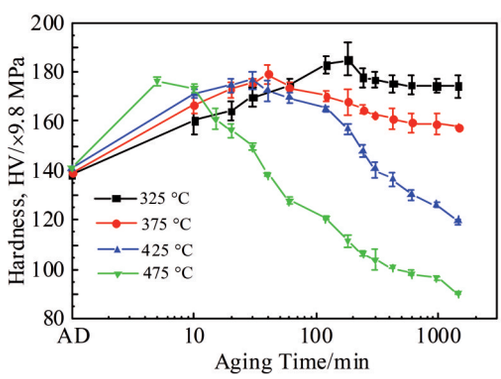


Fig.9 Hardness of alloy specimens after different aging processes

released, and the grains continue to grow, resulting in the decrease in hardness. This is consistent with the results in Ref.[14].

## 3 Conclusions

1) The main phases of the Al-Mn-Mg-Sc-Zr alloy specimen are $\alpha$-Al matrix, $Al_3Sc$ primary phase, and $Al_6Mn$ phase. A large number of fine and dispersed $Al_3Sc$ particles are precipitated in the alloy after aging treatment. The phase relationship between $Al_3Sc$ and $\alpha$-Al phases is $[001]_{Al_3Sc}$// $[001]_{\alpha\text{-Al}}$, and the edge of $Al_6Mn$ phase becomes blunt. $Al_3Sc$ and $Al_6Mn$ phases have good high-temperature stability.

2) The alloy microstructure is mainly composed of equiaxed grains near the fusion line and columnar grains in the center of the molten pool. The average grain size of equiaxed grains in the as-deposited alloy is about 0.57 μm.

3) With the aging treatment proceeding, the alloy hardness is increased firstly and then decreased. When the aging temperature is higher than 375 °C, the hardness loss of alloy after over-aging is large. Compared with that of the as-deposited alloy, the hardness of the alloy after peak-aging (325 °C/180 min) increases by about 30%, reaching 1813.0 MPa.

## References


1 Zhang J L, Song B, Wei Q S *et al. Journal of Materials Science & Technology*[J], 2019, 35(2): 270

2 Chen Y X, Yang Y Q, Feng Z Q *et al. Materials Characterization* [J], 2017, 123: 189

3 Guan Jieren, Chen Chao, Ding Hongyu *et al. The Chinese Journal of Nonferrous Metals*[J], 2022, 32(5): 1224 (in Chinese)

4 Zhu Xi, Yuan Tiechui, Wang Minbu *et al. Materials Science and Engineering of Powder*[J], 2022, 27(2): 205 (in Chinese)

5 Herzog D, Seyda V, Wycisk E *et al. Acta Materialia*[J], 2016, 117: 371

6 Thijs L, Kempen K, Kruth J P *et al. Acta Materialia*[J], 2013, 61(5): 1809

7 Gu Dongdong, Zhang Hongmei, Chen Hongyu *et al. Chinese Journal of Lasers*[J], 2020, 47(5): 32 (in Chinese)

8 Ma Rulong, Peng Chaoqun, Wang Richu *et al. The Chinese Journal of Nonferrous Metals*[J], 2020, 30(12): 2773 (in Chinese)

9 Zhao L, Macías J G S, Ding L P *et al. Materials Science and Engineering A*[J], 2019, 764: 138 210

10 Geng Yaoxiang, Tang Hao, Luo Jinjie *et al. Rare Metal Materials and Engineering*[J], 2021, 50(3): 939 (in Chinese)

11 Xu R, Li R D, Yuan T C *et al. Journal of Alloys and Compounds*[J], 2020, 835: 155 372

12 Lu J L, Lin X, Kang N *et al. Materials Characterization*[J], 2021, 178: 111 305

13 Wang Xiaoguo, Ma Liyun. *Rare Metal Materials and Engineering*[J], 2021, 50(8): 2771 (in Chinese)

14 Jia Q B, Zhang F, Rometsch P *et al. Acta Materialia*[J], 2020, 193: 239

15 Cui Xiaoming, Meng Chuang, Shi Bo *et al. Rare Metal Materials and Engineering*[J], 2022, 51(7): 2529 (in Chinese)


# 热处理前后选区激光熔化 Al-Mn-Mg-Sc-Zr 合金微观组织的演变


崔晓明，梁绍波，赵学平，崔　昊，刘　飞，杜赵新，白朴存

(内蒙古工业大学 材料科学与工程学院，内蒙古 呼和浩特 010051)



**摘　要：**采用选区激光熔化（SLM）技术制备了 Al-Mn-Mg-Sc-Zr 合金。使用 X 射线衍射仪、扫描电子显微镜、能谱仪和透射电子显微镜等测试方法，表征了热处理前后 Al-Mn-Mg-Sc-Zr 合金微观组织的结构，并测试了合金的硬度。结果表明：沉积态合金组织主要由 $\alpha$-Al、$Al_6Mn$ 和初生 $Al_3Sc$ 组成。SLM 成形的合金熔池组织呈鱼鳞状，熔池内靠近熔合线附近形成了大量细小的等轴晶，平均晶粒尺寸约为 0.57 μm，熔池心部则由柱状晶组成，柱状晶的平均宽度约为 0.48 μm。棒状 $Al_6Mn$ 主要沿晶界分布，少量颗粒状的初生 $Al_3Sc$ 存在于晶粒内部，这表明初生 $Al_3Sc$ 可以作为异质形核质点，细化 $\alpha$-Al 基体。热处理后，熔池内部等轴晶尺寸及柱状晶宽度均有所增大，组织中析出了大量细小弥散的二次 $Al_3Sc$ 颗粒。硬度测试结果表明，随着时效时间的延长，各温度条件下合金的硬度值呈先升高后降低的趋势，相比于沉积态合金的硬度，在 325 ℃、180 min 时效热处理后合金的硬度提高了 30% 左右，达到 1813.0 MPa。



**关键词：**Al-Mn-Mg-Sc-Zr 合金；选区激光熔化技术；稀土 Sc；热处理；微观组织


---


作者简介：崔晓明，男，1981 年生，博士，副教授，内蒙古工业大学材料科学与工程学院，内蒙古 呼和浩特 010051，电话：0471-6575752，E-mail：xmcui@imut.edu.cn